Contents lists available at ScienceDirect

Icarus

journal homepage: www.elsevier.com

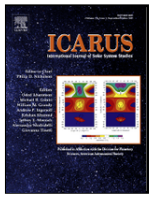

Evidence for ultra-cold traps and surface water ice in the lunar south polar crater Amundsen

E. Sefton-Nash [a, *], J.-P. Williams [b], B. T. Greenhagen [c], T. J. Warren [d], J. L. Bandfield [e], K.-M. Aye [f], F. Leader [g], M. A. Siegler [h], P. O. Hayne [i], N. Bowles [d], D. A. Paige [b]

[a] European Space Research and Technology Center (ESTEC), European Space Agency, 2200 AG Noordwijk, the Netherlands
[b] Department of Earth, Planetary and Space Sciences, University of California Los Angeles, 595 Charles Young Drive East, Box 951567, Los Angeles, CA 90095-1567, USA
[c] Johns Hopkins University Atmospheric Physics Laboratory, 11101 Johns Hopkins Road, Laurel, MD 20723, USA
[d] Atmospheric, Oceanic and Planetary Physics, University of Oxford, Department of Physics, Clarendon Laboratory, Parks Road, Oxford OX1 3PU, United Kingdom
[e] Space Science Institute, 4750 Walnut Street, Suite 205, Boulder, CO 80301, USA
[f] Laboratory for Atmospheric and Space Physics (LASP), 3665 Discovery Drive, Boulder, CO 80303, USA
[g] Jet Propulsion Laboratory, California Institute of Technology, Pasadena, CA 91109, USA
[h] Planetary Science Institute, 1700 East Fort Lowell, Suite 106, Tucson, AZ, USA
[i] Astrophysical & Planetary Sciences, University of Colorado Boulder, 391 UCB, 2000 Colorado Ave, Boulder, CO 80309, USA

ARTICLE INFO

Keywords:
Moon
Permanent shadow
Polar
Volatiles
Emissivity

ABSTRACT

The northern floor and wall of Amundsen crater, near the lunar south pole, is a permanently shaded region (PSR). Previous study of this area using data from the Lunar Orbiter Laser Altimeter (LOLA), Diviner and LAMP instruments aboard Lunar Reconnaissance Orbiter (LRO) shows a spatial correlation between brighter 1064 nm albedo, annual maximum surface temperatures low enough to enable persistence of surface water ice (< 110 K), and anomalous ultraviolet radiation. We present results using data from Diviner that quantify the differential emissivities observed in the far-IR (near the Planck peak for PSR-relevant temperatures) between the PSR and a nearby non-PSR target in Amundsen Crater.

We find features in far-IR emissivity (50–400 μm) could be attributed to either, or a combination, of two effects (i) Differential regolith emissive behavior between permanently-shadowed temperature regimes and those of normally illuminated polar terrain, perhaps related to presence of water frost (as indicated in other studies), or (ii) high degrees of anisothermality within observation fields of view caused by doubly-shaded areas within the PSR target that are colder than observed brightness temperatures.

The implications in both cases are compelling: The far-IR emissivity curve of lunar cold traps may provide a metric for the abundance of "micro" cold traps that are ultra-cool, i.e. shadowed also from secondary and higher order radiation (absorption and re-radiation or scattering by surrounding terrain), or for emissive properties consistent with the presence of surface water ice.

1. Introduction

Permanently shadowed regions (PSRs) persist at the lunar poles due to the Moon's low axial tilt. Crater interiors and other topographic depressions act as cold traps and may host conditions suitable for long-term stability of surface or subsurface volatiles. The predominant sources of radiation in PSRs are limited to upwelling heat flow from the lunar interior, stellar radiation, secondary illumination by reflected or scattered light from illuminated surfaces, or thermal emission from nearby warmer shadowed surfaces. These radiative sources are often negligible, allowing PSRs to remain at very low temperatures that are more akin to those observed on bodies in the outer solar system.

Recent studies of the lunar poles using data from NASA's Lunar Reconnaissance Orbiter (LRO) have focussed on isolating potential signatures of such volatiles, following the detection by the Lunar Crater Observation and Sensing Satellite (LCROSS) (Schultz et al., 2010) of water

* Corresponding author.
Email address: e.sefton-nash@cosmos.esa.int (E. Sefton-Nash)

https://doi.org/10.1016/j.icarus.2019.06.002
Received 2 October 2018; Received in revised form 17 May 2019; Accepted 3 June 2019
Available online xxx
0019-1035/

and other volatiles in a plume of material ejected from Cabeus crater by the impact of a spent rocket stage (Colaprete et al., 2010). The body of results to date does not conclusively resolve the distribution of volatile abundance at the surface, nor in near-surface regolith layers. However, work to determine the presence of surface volatiles in the lunar South Polar region is generally consistent with laterally discontinuous veneers of water ice (Hayne et al., 2014, 2015; Fisher et al., 2017, Li et al., 2018).

We analyse far-IR data from the South Polar Amundsen crater to explore the differences in far-IR emission, as observed by the Diviner Lunar Radiometer Experiment aboard LRO (Paige et al., 2010a). We select a partially illuminated target as a control (i.e. where we would not expect to find evidence for surface volatiles due to the high daytime temperatures), and a permanently shadowed target identified as a high priority site for study of lunar volatiles (Lemelin et al., 2014), and in which there is evidence in remote sensing data for surface water ice (Hayne et al., 2015; Fisher et al., 2017).

2. Targets in Amundsen crater

Compared to other major south polar PSRs, the PSR in Amundsen crater offers the advantage of being predominantly outside the reduced observation coverage in polar regions. This is caused by a combination of a reduction in LRO's orbit inclination 2009–2016, and the nominal nadir pointing of Diviner.

We define target boundaries at a 3 km radius around centers of 93.1047°E, 84.5523°S and 91.2826°E, 83.6889°S for non-PSR (NPSR) (i.e. partially illuminated) and permanently shadowed (PSR) targets, respectively (Fig. 1). For the PSR target this radius ensures that only observations from within the PSR boundary are included, but the size is also a balance between minimizing area (to minimize scatter caused by heterogeneous thermal states) and ensuring sufficient data coverage for robust statistics, and computational capabilities.

Our permanently shadowed target includes terrain that is reported as having both surface temperatures and local slopes low enough to enable persistence of surface water ice (<110 K and <10° respectively), and brighter 1064 nm albedo, as measured by Lunar Orbiter Laser Altimeter (LOLA) reflectance (Fisher et al., 2017). However, not all permanently shadowed areas, and only a portion of our PSR target, show this correlation between bright 1064 nm albedo and low temperatures.

A similar correlation was performed by Hayne et al. (2015) between annual maximum temperature and anomalous ultraviolet radiation as measured by the Lyman Alpha Mapping Project (LAMP) (Gladstone et al., 2010). In that study, UV spectra of PSRs were obtained by measuring reflectance of starlight and emission from interplanetary hydrogen. The spectral features of water-ice in the UV were characterized by LAMP by observing (i) decreasing albedo in the 129.57–155.57 nm bandpass, (ii) increasing albedo in the 155.57–189.57 nm bandpass, and (iii) decreasing Lyman-alpha albedo (199–125 nm). The ratio of the first bandpasses, known as the "off-band/on-band" ratio (referring to the contrasting UV spectral features of water frost in those regions), was shown to be consistent with the presence of water ice layers >~100 nm thick at locations where maximum surface temperatures never exceed 110 K. One such location is a patchy distribution of areas in the permanently shaded portion of Amundsen crater, which show a combination of off/on-band ratios >1.2 and Lyman-α albedo <0.03, indicating a possible water mass content of 0.1–2.0% (Hayne et al. 2015).

Some of these patches are contained within our PSR target, but do not completely coincide with areas that also show high 1064 nm albedo (compare Hayne et al., 2015, Fig. 14 and Fisher et al., 2017, Fig. 11). Thus, while there is not complete overlap between these signatures, portions of our selected PSR target indicate annual maximum temperatures, as well as ultraviolet and near-IR signatures that are anomalous compared to other south polar terrain in permanent shadow, and are consistent with the presence of surface water frost. Our method intends to quantify any effect by the presence of water frost, or by ultra-low temperatures, on emissivity of these terrains in the far-IR, near their Planck peak (λ_{max}).

2.1. Observations

LRO's orbit configuration allows opportunities for nadir observation of the two targets approximately every two weeks, alternating between the day and night side. We retrieve all observations of both targets for the duration of the mission (July 2009–August 2017) and constrain them to emission angles <5° to minimize off-nadir effects.

We process observations from Diviner channels 7, 8 and 9, which are sensitive to photons between approximately 25–41, 50–100 and 100–400 μm respectively, and most representative of surface brightness temperatures between 59 and 178, 43–69, and <43 K respectively (Paige et al., 2010a). These data provide sufficient spectral coverage of radiance due to the expected nighttime temperatures. Data from channel 6 was found to be not useful due to the channels very low sensitivity to PSR-relevant temperatures (predominantly sensitive to ≳178 K), and was therefore not included in this study.

For the two targets we plot brightness temperatures for Diviner channels 7, 8, and 9 as a function of local mean solar time (LMST) (Fig. 2). The large spread of brightness temperatures is expected to be due to the high dynamicity of diurnal and seasonal illumination conditions experienced by polar terrain, that are heavily dependent on local topography causing shadows. This is particularly evident in the discontinuous distribution in daytime temperatures for the partially illuminated target (Fig. 2). Causes of the spread in apparent nighttime brightness temperatures for both targets could include secondary emission from illuminated or warmer terrain, as well as be due to differences in surface temperature and emissivity. For the non-permanently shadowed target, residual energy imparted by direct daytime illumination is also a likely contributor.

3. Method

We aim to determine the distribution and extent of terrain that contributes to signal received by Diviner's long wavelength channels as fully and precisely as possible. To quantify the emitting surface area that contributes to the radiance recorded in each observation, we begin with the boresight of each observation, defined by the latitude and longitude of intersection with a lunar sphere of radius 1,737,400 m (Seidelmann et al., 2002).

Following Williams et al. (2016), we model the effective field-of-view (EFOV) as a probability distribution of signal that accounts for the instantaneous field-of-view, detector lag, and spacecraft motion during integration time. Details on how the Monte Carlo points that comprise each EFOV are transformed from instrument-relative to lunar body fixed coordinates, such that they can be projected onto a lunar digital elevation model (DEM), are described in Appendix A.

With the EFOV modelled as discrete rays connecting the lunar surface to the detector, we perform ray-tracing according to Teanby (2006) to determine the point of origin in the DEM from which each EFOV point originates. As an extension to the method for processing global gridded data records from modelled EFOVs described in Williams et al. (2016), our technique additionally allows processing of high emission angle observation geometries.

Due to the nature of the processing pipeline a case exists where observations or partial observations may be excluded from analysis when the boresight of a very high emission angle observation (≳80°) does not intersect with the lunar sphere, but a fractional part of the EFOV of the observation does, e.g. the boresight passes the lunar limb, but e.g. a

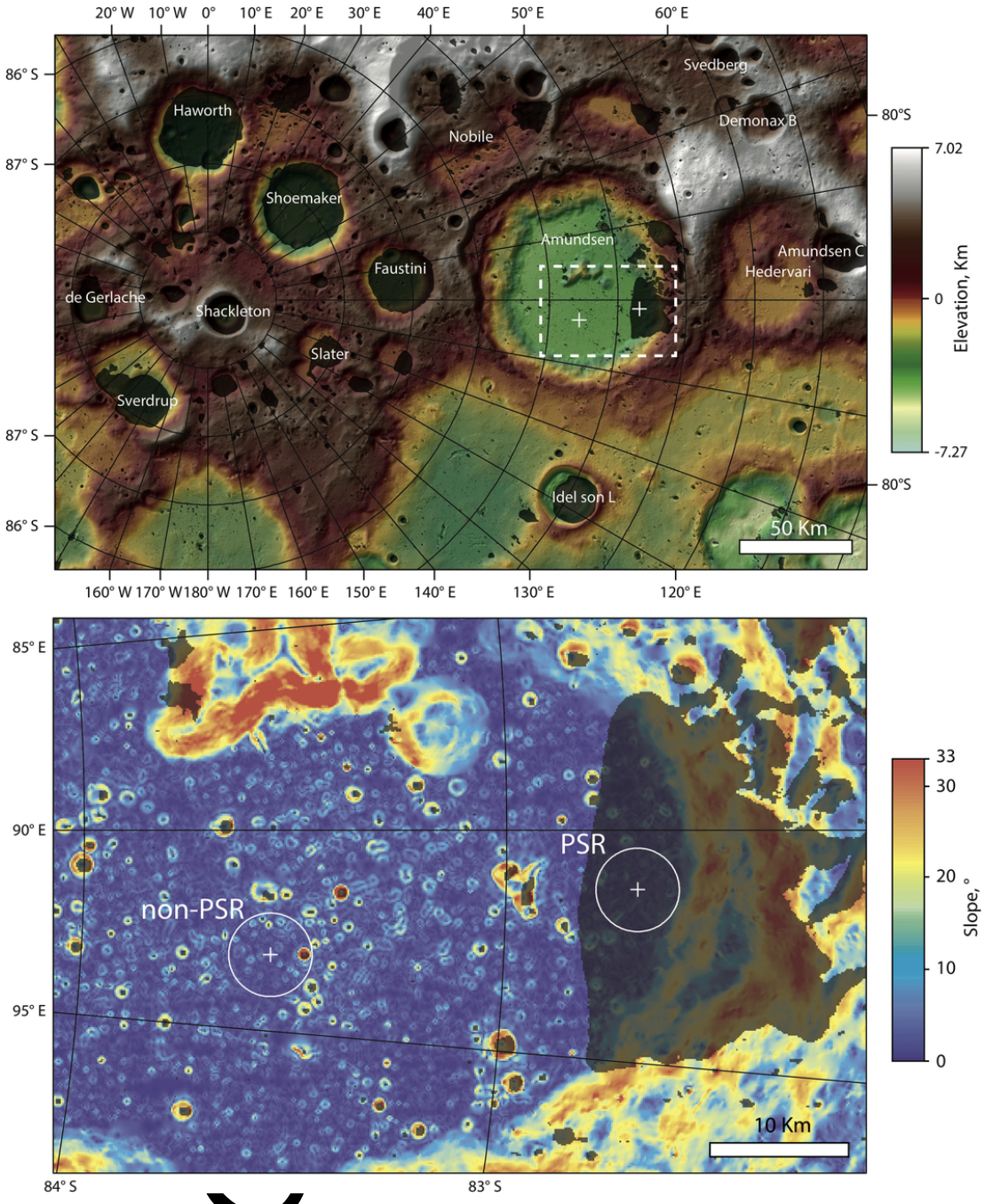

Fig. 1. Top – Lunar south polar region in stereographic projection illustrated with colorized hillshade of LOLA elevation at 20 m/pixel ('LDEM_80S_20M_FLOAT'). Regions in permanent shadow calculated at 120 m/pixel (Mazarico et al., 2011) are plotted as darkened areas ('LPSR_75S_120M_201608'). Named craters are labeled and the white dashed box marks the area plotted in the lower panel. The two targets in Amundsen crater are marked with a white '+'. Bottom – Slope map at 120 m/pixel of the study region ('LDSM_75S_120M'). A 3 km radius from the targets is marked, and used to delineate observations of target areas from those of the surrounding terrain. (For interpretation of the references to color in this figure legend, the reader is referred to the web version of this article.)

mountain beyond the horizon has a peak appearing above the horizon that contributes some signal. In these cases the whole observation is excluded. However, coverage of the targets by the available data at high emission angles is poor (see Section 5.3).

The terrain model is produced as follows: A triangular mesh is first generated on a lunar sphere of radius 1737.4 km (Seidelmann et al., 2002) using the icosahedron subdivision generation method of Teanby (2006). Vertices result from 12 iterative bisections of icosahedron edges, corresponding to a mean on-sphere vertex separation of ~560 m and triangle area of ~0.14 km^2 (Sefton-Nash et al., 2017). Slopes below this scale are not resolved, but the mesh resolution is on the order of the size of Diviner observation footprint. After generation of mesh vertices on the lunar sphere, vertices are adjusted in the vertical direction by retrieving the elevation at each vertex's on-sphere position via interpolation of the LOLA gridded data record LDEM_60S_60M.IMG (Smith, 2017) using Delaunay Triangulation (Delaunay, 1934).

At high emission angles, ground-projected EFOVs are extended in the horizontal direction of the look vector, including distal terrain that may be of significantly different radiative state. This sometimes results in the location of maximum probability, i.e. where the peak magnitude

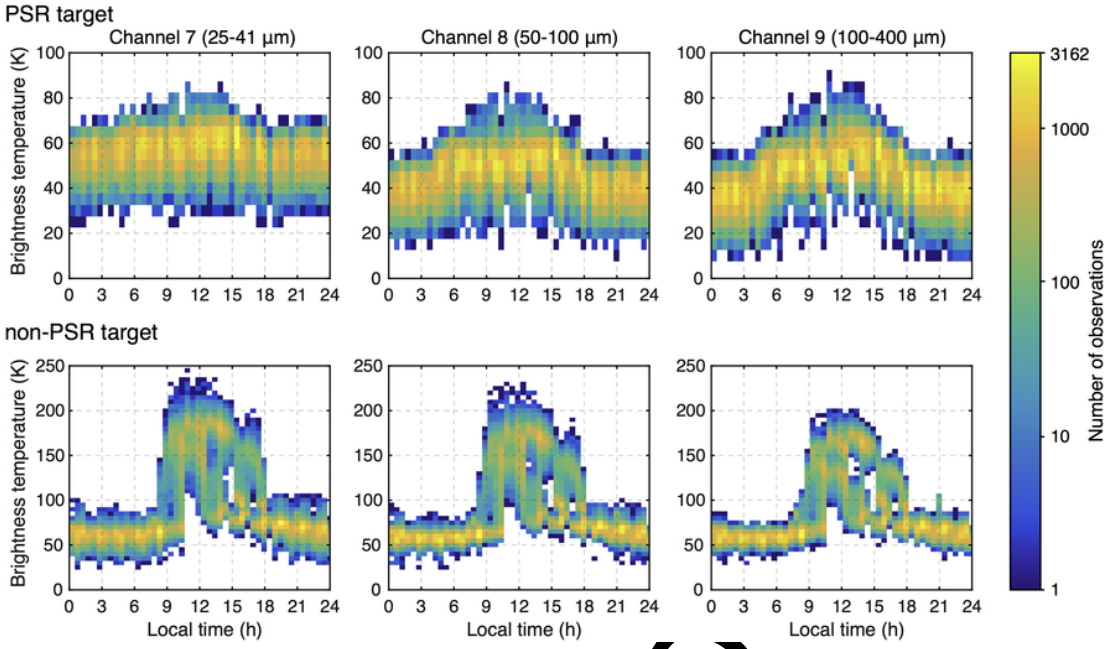

Fig. 2. 2D histograms of brightness temperatures observed for the permanently shadowed (top) and partially illuminated (bottom) targets over the duration of the LRO mission (July 2009–August 2017), and plot as a function of local mean solar time (LMST). To best illustrate structure in the distributions we have selected to display the number of observations (on a log color scale) in bins of 5 K and 0.5 h. To reduce off-nadir effects data with boresight emission angles $<5°$ are omitted. (For interpretation of the references to color in this figure legend, the reader is referred to the web version of this article.)

of the signal originates, being significantly offset from the boresight intersection with the surface. To minimize potential scatter, we therefore discount observations where the location of peak EFOV probability intersects with terrain outside the target radius.

Conversely, we also account for observations whose boresight terrain intersections may lie outside the target radius, but whose maximum EFOV probability lies inside. This is accomplished by initially calculating EFOVs for data whose boresight intersection is within 5 km, then including any with an EFOV maximum that lies within 3 km.

For each of the Diviner thermal channels 7, 8 and 9 (selected for their sensitivity to PSR and nighttime temperatures), an area-weighted average of radiance was calculated for each triangle in the terrain model where observations in each orbit track intersect with it. Observations within one orbit are spaced closely enough in time (<1 s) that effectively they represent the same surface radiative state. Therefore we bin observations from the three relevant thermal channels on a per orbit basis such that they may be associated. To illustrate the cumulative result of this process, we plot the total number of observations made by channel 9 of the two targets on a per triangle basis (Fig. 3). In general, more observations were acquired of the non-PSR target (~8500–9200 per triangle) than for the PSR target (~7200–8200 per triangle), and mild heterogeneity in spatial coverage of the two target areas is evident. We propagate the number of observations as a function of various parameters in our analysis in order to highlight any potential observation bias.

Radiance, $\mathfrak{R}$, received in a channel, c, is described by:

$$\mathfrak{R}_c = \int_{\lambda_1}^{\lambda_2} \varepsilon(\lambda)\, f_c(\lambda)\, B\left(T_s, \lambda\right)\, d\lambda$$

where $f_c(\lambda)$ and $\varepsilon(\lambda)$ are the quantum efficiency and emissivity at wavelength λ, respectively, B is the black body radiance emitted at wavelength λ, by a surface of temperature, T_s. Wavelength limits on integration, λ_1 and λ_2 encompass the range for which quantum efficiency data are available (Paige et al., 2010a) for each channel. This formulation ignores emission angle effects.

For a given observation geometry, we may make two important assertions: Firstly, the quantum efficiency as a function of wavelength, $f_c(\lambda)$, is constant and known for each channel (Paige et al., 2010b). Secondly, $B(T_s, \lambda)$ may be assumed constant for a fixed location that is observed by Diviner in a single orbit pass. Diviner's integration time is 0.128 ms and the resulting time differential between successive observations between channels with overlapping EFOVs is <1 s. Changes in the radiative state of the surface are therefore unlikely over the course of a few integration times, and consequently the surface kinetic temperature, T_s, is assumed fixed during an orbit pass.

Typically for each orbit, co-aligned observations from all three long wavelength thermal channels (7, 8 and 9) are coincident on the DEM. In these cases, where radiance is recorded in multiple spectral bandpasses, we may approximate T_s with the bolometric brightness temperature, T_{BOL} (Paige et al., 2010a). T_{BOL} is retrieved from a black body spectrum that is fit to observed radiance integrated over multiple bandpasses. Importantly, this is performed for every terrain element that contributes signal in the orbit swath. T_{BOL} is, by definition, a brightness temperature, in that it assumes black body emission i.e. it includes the cumulative effects of any dependence of emissivity on temperature or wavelength.

The orientation and position of each terrain element produces an individual observation geometry, an important parameter of which is the terrain relative emission angle. Therefore, for each terrain element, i.e. triangle in the DEM, that is observed, and over many orbits, we generate a large list of data points to populate a parameter space with dimensions: T_{BOL}, $\mathfrak{R}_7$, $\mathfrak{R}_8$, $\mathfrak{R}_9$, local time and terrain relative emission angle.

4. Results

Observed radiance includes any effects of variation in emissivity as a function of local time, emission angle or bolometric temperature. Consequently, without independent constraint of $\varepsilon(\lambda)$ in any channel

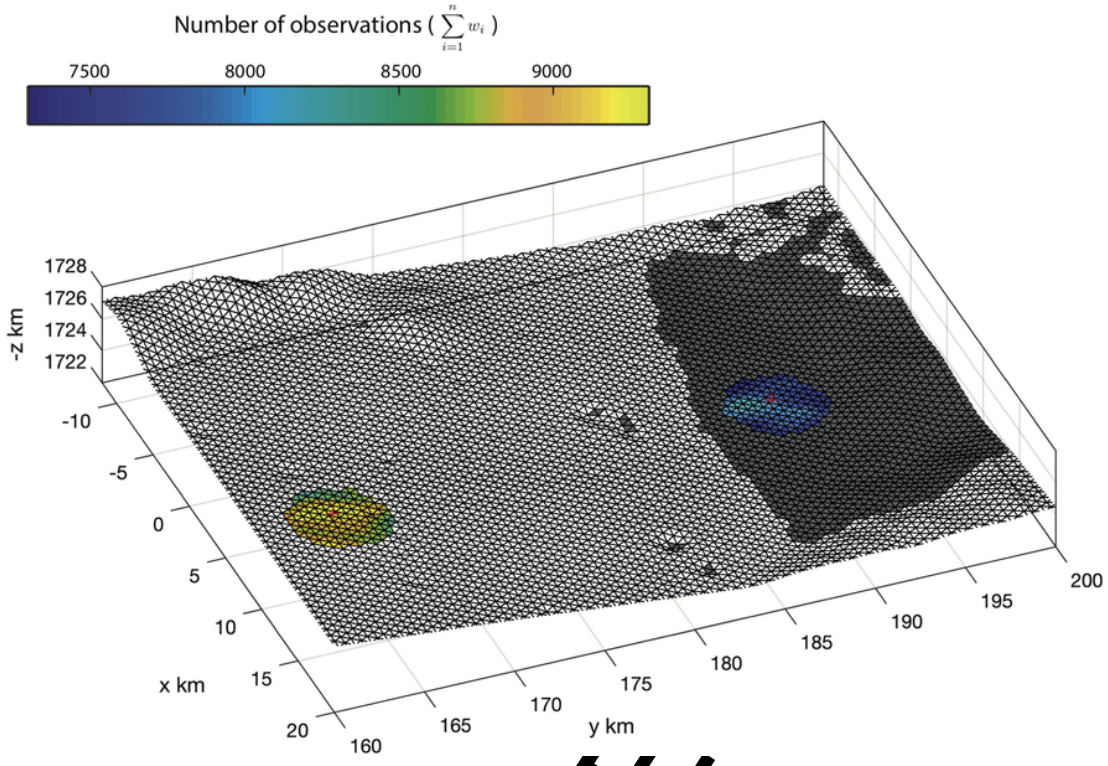

Fig. 3. Demonstration of projection of EFOVs onto the terrain model. The cumulative number of observations by Diviner channel 9 (all detectors) within 3 km radius of the PSR and NPSR targets. Triangles that are shaded gray have all three vertices in permanent shadow according to the permanent shadow map produced by Mazarico et al. (2011). Red crosses mark target centers. (For interpretation of the references to color in this figure legend, the reader is referred to the web version of this article.)

we cannot deconvolve the effects of surface kinetic temperature from apparent emissivity using only radiance received in a single channel.

With two bandpasses, however, we may calculate the relative change in apparent emissivity. Using this rationale, we investigate the ratio of radiance received in Diviner channels 8 and 9, $\mathfrak{R}_{8/9}$, for the permanently shadowed and partially illuminated target. Due to the fact that T_{BOL} is calculated using radiance from channels 7, 8 and 9, regressing the ratio $\mathfrak{R}_{8/9}$ against T_{BOL} reduces self-dependencies that could be introduced by instrumental effects if only channels 8 and 9 were used to calculate T_{BOL}.

However, while interesting trends may be observed in this apparent correlation between $\mathfrak{R}_{8/9}$ and bolometric temperature (Fig. 4), they are not meaningful in terms of extracting information on apparent emissivity unless we understand what value of $\mathfrak{R}_{8/9}$ should be expected as a function of surface kinetic temperature. We must account for the convolution of Diviner's spectral bandpasses with radiance from thermal emission.

4.1. Band ratio model

To address this we model radiance expected as a function of surface kinetic temperature using T_{BOL}. We calculate expected radiance from a black body by multiplying Diviner's quantum efficiency for each channel by the black body curve $f(\lambda)\ B\ (T_S, \lambda)$ (Fig. 5, left, middle). Over a PSR-relevant range of T_S (0–200 K), and for each Diviner channel, we integrate beneath these curves to model radiances expected for a black body (ε is not wavelength dependant and always equal to unity):

$$\mathfrak{R}_{c,model} = \varepsilon \int f_c(\lambda)\ B\left(T_S, \lambda\right)\ d\lambda$$

Ratios between these integrated radiances are plotted as a function of temperature (Fig. 5, right). We select channels 8 and 9 for this investigation, as they are most sensitive to PSR-relevant temperatures and allow us to best explore the ultra-low temperature regime of the PSR target.

For the observed band ratio, $\mathfrak{R}_{8/9}$, we permit wavelength-dependent emissivity, $\varepsilon(v)$. The modelled band ratio $\mathfrak{R}_{8/9\ model}$, can therefore be compared to the observed $\mathfrak{R}_{8/9}$:

$$\mathfrak{R}_{8/9} - \mathfrak{R}_{8/9\ model} = \frac{\int \varepsilon(\lambda)\ f_8(\lambda)\ B\left(T_S, \lambda\right)\ d\lambda}{\int \varepsilon(\lambda)\ f_9(\lambda)\ B\left(T_S, \lambda\right)\ d\lambda} - \frac{\int f_8(\lambda)\ B\left(T_{BOL}, \lambda\right)\ d\lambda}{\int f_9(\lambda)\ B\left(T_{BOL}, \lambda\right)\ d\lambda}$$

Assuming that bolometric brightness temperature is a valid representation of surface kinetic temperature, i.e. $T_{BOL} = T_S$, then the difference between the two is influenced only by any differences in $\varepsilon(\lambda)$ that might exist between the apparent emissivity integrated over the bandpasses of each channel.

In our formulation, with $\mathfrak{R}_8$ as the numerator, a positive value of $\mathfrak{R}_{8/9}$ implies that emission received by channel 8 increases relative to that in 9, or conversely that emission received in channel 9 decreases relative to that in 8. Consequently, because $\mathfrak{R}_{8/9\ model}$ represents a black body where emissivity is therefore constant at all wavelengths, a positive value of $\mathfrak{R}_{8/9} - \mathfrak{R}_{8/9\ model}$ corresponds to an under-prediction by the model of the apparent relative increase in emissivity over the channel 8 bandpass compared to that in 9, or vice versa, i.e.:

$$\int \varepsilon(\lambda)\ f_8(\lambda)\ d\lambda > \int \varepsilon(\lambda)\ f_9(\lambda)\ d\lambda$$

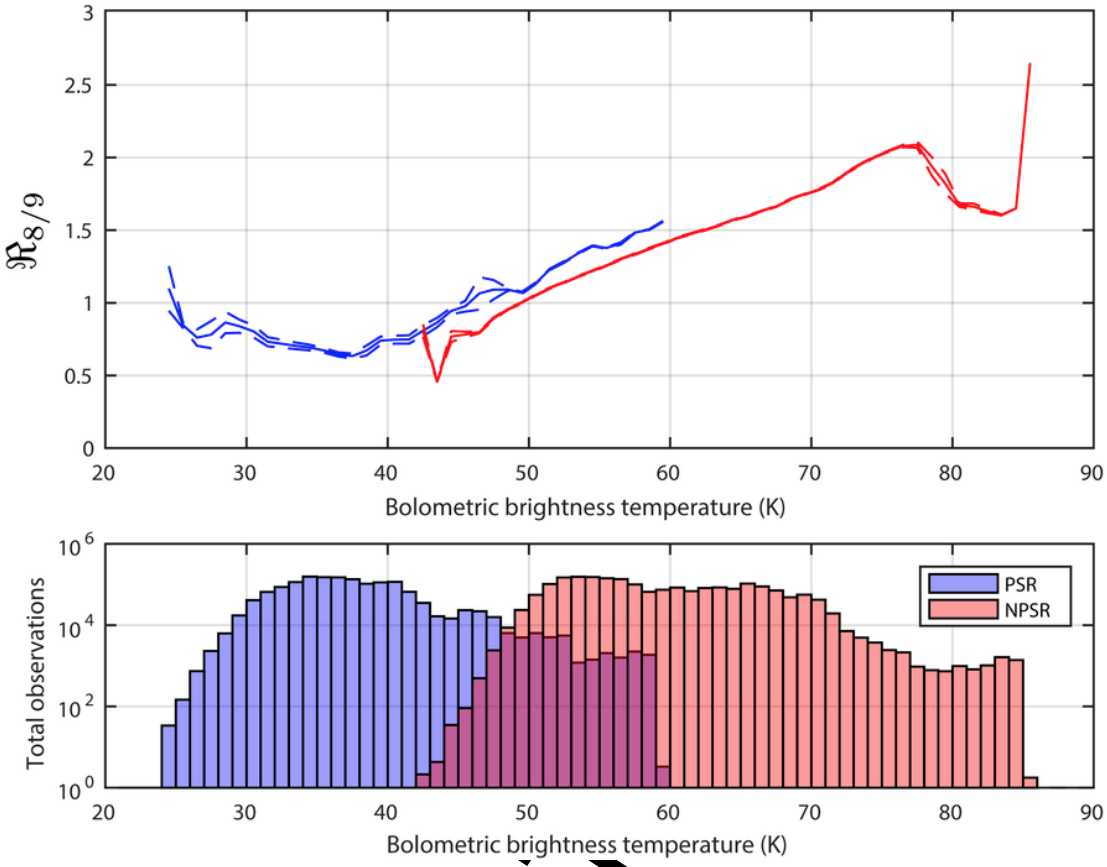

Fig. 4. Top – Weighted mean $\Re_{8/9}$ as a function of bolometric brightness temperature, T_{BOL}. Dashed lines for the PSR (blue) and NPSR (red) curves represent the standard deviation on the distribution of $\Re_{8/9}$ at each value of T_{BOL}. Bottom – Total number of observations (sum of observations in channels 8 and 9), plotted as a function of T_{BOL} in bins of 1 K. (For interpretation of the references to color in this figure legend, the reader is referred to the web version of this article.)

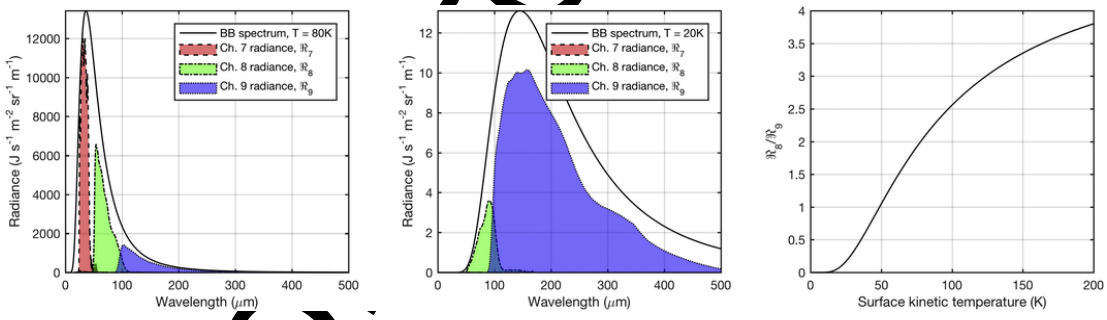

Fig. 5. Left: Spectrum for a black body at 80 K with bandpasses of Diviner channels 7 (red), 8 (green) and 9 (blue) integrated beneath it. The ratio of signal contribution between channels 8 and 9 in this case, $\Re_{8/9} = 2.06$. Center: Similarly, spectrum emitted by a black body at 20 K and the corresponding integrated contributions from channels 7, 8 and 9. At this low temperature, emitted radiance is about a factor of 10^{-6} lower than at 80 K, but the signal is dominated by channel 9, with $\Re_{8/9} = 0.07$. Right: $\Re_{8/9}$ plotted as a function of black body surface kinetic temperature. Channel 9 radiance becomes the dominant signal for surface kinetic temperatures below ~50 K, while above this channel 8 is dominant. (For interpretation of the references to color in this figure legend, the reader is referred to the web version of this article.)

With this rationale established, we plot the mean $\Re_{8/9} - \Re_{8/9\ model}$ against bolometric brightness temperature that we observe for the PSR and NPSR targets (Fig. 6), as well as a 1-sigma envelope.

The greatest concentrations of observations cover different temperature domains for the two targets, due to their different nighttime temperature regimes (Fig. 2). The largest number of observations for the PSR target is between ~32–40 K, and observation density is seen for the NPSR target between ~50–70 K (Fig. 6). We deem these temperature intervals therefore to be the least susceptible to any remaining observation bias in other parameters that correlate with temperature. We explore possibility of observation bias due to emission angle or local time coverage in the Discussion section.

For the NPSR target, importantly we see that in the temperature domain with the strongest statistics, ~50–70 K, observations are almost perfectly predicted by our model, i.e. $\Re_{8/9} = \Re_{8/9\ model}$. This implies that relative emissivities integrated over the two channels are equal, though not necessarily 1, as in the black body model. It also implies that relative emissivities between the channels stay constant over this temperature range.

A small upturn around 75 K and subsequent dramatic downturn from ~77 K upwards both coincide with reduced numbers of observations, and therefore more susceptible to observation bias. Consequently, we do not interpret these features as having significant physical meaning.

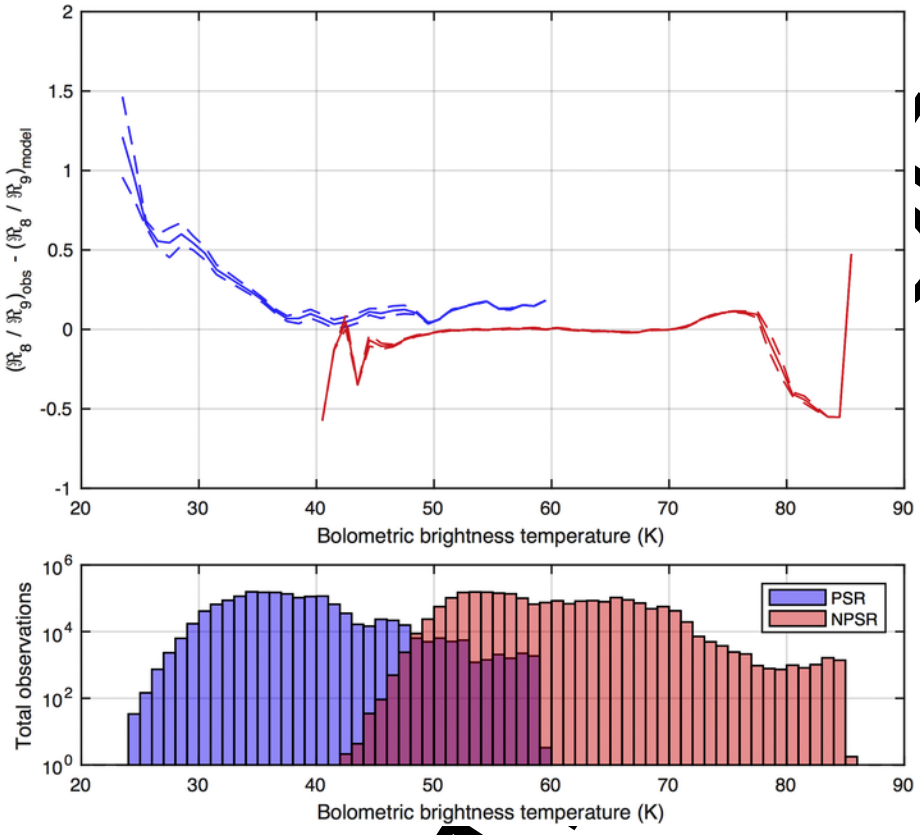

Fig. 6. Top – $\Re_{8/9}$ - $\Re_{8/9\_model}$ as a function of bolometric brightness temperature for each target. Dashed lines indicate a 1?? envelope. Bottom – Total number of observations in both channels 8 and 9 (log scale) for each target, plotted as a function of T_{BOL} in bins of 1 K.

For the PSR target we see different emissive behavior. For the temperature region between 40 K to ~60 K, $\Re_{8/9} - \Re_{8/9\ model}$ is non-zero and higher than that for the NPSR target. Implying that different emissivities are measured in the two bandpasses. However, this temperature range suffers from reduced numbers of observations compared to the NPSR target, decreasing to just a few hundred observations per K towards 60 K, so this result should be interpreted with caution.

Most importantly for the target in permanent shadow, between 30 and 40 K where observation density is highest (a few 10^5 observations per bin; equivalent to the highest data densities for the NPSR target), a slope is seen in relative emissivity between channels 8 and 9: $\Re_{8/9} - \Re_{8/9\ model}$ appears to increase with decreasing temperature in this range.

This major result implies a temperature-dependent apparent emissivity in far-IR for the PSR target. Either, emissivity between 50 and 100 μm increases relative to 100–200 μm, or emissivity over the longer wavelength bandpass decreases relative to that in the shorter.

5. Discussion

5.1. Far-IR spectral features of water ice

To explore possible interpretations of our observations, we first consider the far IR spectral features of water ice, and the likelihood of their role in the above results. Amorphous water-ice has a broad absorption peak near 45 μm, while crystalline ice has absorptions near 44 μm and 62 μm (Moore and Hudson, 1992). The sensitivity and spectral coverage of Diviner channels 7 and 8 might permit detection of these features, though complexities are introduced by the presence of silicates. Absorption is sensitive to grain size, crystallinity, contaminants and the porosity of water ice (Hayne et al., 2014, Carvano et al., 2006). The bands at 44–45 are most likely to yield a detection for spectral mixtures of ice and regolith, however this region is poorly detectable by Diviner because it is located near the upper sensitivity boundary of channel 7 (~41 μm), but lower sensitivity boundary of channel 8 (~50 μm) (Paige et al., 2010a, 2010b). In PSRs where surface water frost is most likely to be present, temperatures are coldest and thus measurements more challenging. Consequently, more spectral channels with narrower bandpasses and higher sensitivity would probably be needed to distinguish these features from thermal emission from ice-poor lunar regolith.

5.2. Sub-FOV thermal heterogeneity due to roughness

Accepting that composition-based spectral features of water ice are not likely to significantly contribute to the signal we observe, we next consider the possible effects of surface roughness in PSRs, as has been quantified using in TIR observations over the lunar globe (Bandfield et al., 2015). Sub-FOV scale "micro" doubly-shadowed cold traps, topographic lows in PSRs that are also protected from secondary and higher order thermal emission (e.g. from crater walls), may contribute to anisothermality in PSRs. We construct a simple model that considers radiance contributions from a bi-modal brightness temperature distribution. The black body emission at wavelength λ from two bodies at temperatures, T_1 and T_2, may be described by:

$$\Re_{total}(\lambda) = aB(T_1, \lambda) + (1 - a)B(T_2, \lambda)$$

where $\Re_{total}(\lambda)$ is the total radiance and a is the fraction of the radiance originating from the body at temperature T_1. Multiplying $\Re_{total}(\lambda)$ with the quantum efficiencies of each channel (f_8 and f_9) and integrating over wavelength, we retrieve the expected band ratio for the ther-

mal emission spectrum modelled for a bimodal temperature distribution:

$$\Re'_{8/9} = \frac{\int f_8(\lambda)\ \Re_{total}(\lambda)\, d\lambda}{\int f_9(\lambda)\ \Re_{total}(\lambda)\, d\lambda}$$

T_1 represents the temperature of the double permanently shadowed terrain, and is varied between 15 and 40 K. T_2 represents the temperature of the single permanently shadowed terrain, which we fix at 40 K, typical for the PSR target (Fig. 2).

Subtracting the band ratio modelled for the bimodal temperature distribution, $\Re'_{8/9}$, from that for a uniform temperature distribution at 40 K (Fig. 7) permits us to assess the potential effects that sub-FOV doubly-shadowed terrain could have on band ratios.

We plot the difference between $\Re_{8/9}$ expected for observations of terrain at 40 K and that for the same terrain with some fraction at a lower temperature $\Re'_{8/9}$, due to its double-shadowing. We vary both the fraction of colder terrain (from 0.4 to 1) and its temperature from 15 to 40 K. Fig. 8 shows the difference is larger when anisothermality and fraction of doubly shadowed terrain is greatest, but can also reduce for moderate fractions (~0.5–0.8) of very cold (~15–25 K) doubly shadowed terrain. This is due to the non-linearity of Planck emission to the signal with decreasing temperature. We acknowledge the model described considers a bimodal temperature distribution, and that a realistic temperature distribution would be required to fully assess the possible magnitude of this effect for real observations. Nonetheless, it is clear that terrain with brightness temperatures of ~40 K, such as the PSR target (Fig. 2), could produce anisothermality observable in the far-IR if doubly-shadowed terrain occupies modest significant fractions of FOVs. Indeed, Fig. 6 indicates values of $\Re_{8/9} - \Re_{8/9\ model}$ of 0–0.5 between 30 and 40 K, where statistics are best. Such values could be produced if PSR terrain at 40 K contains more than about 0.4 areal fraction of terrain that is up to ~15 K cooler (Fig. 7).

Modelling by Rubanenko and Aharonson (2017) [Fig. 9c] suggests that terrains with high RMS slope (σ_S) distributions produce higher cold-trap areal fractions, and by the same principle could also produce higher areal fractions of doubly-shadowed PSRs. For synthetically generated terrains with Gaussian slope distributions and at the approximate latitude of the two targets in this study (~87.5° S) $\sigma_S = 25°$ permits PSR areal fractions of up to ~0.45, and relatively smooth surfaces ($\sigma_S = 10°$) are required for PSR areal fractions of up to ~0.3.

Therefore the apparent temperature dependence shown in Fig. 6 could be caused by binning of observations as a function of temperature, such that lower apparent temperatures are observed for areas with higher areal fractions of double-PSRs in the FOV. For the apparent temperature range 30–40 K, this suggests our observations of the PSR could be consistent with it containing modest to rough surfaces comparable in RMS slope distribution to those derived for global lunar TIR observations (Bandfield et al., 2015).

However, it is unlikely that this effect could be sufficient to produce the high values of $\Re_{8/9} - \Re_{8/9\ model}$ observed for temperatures ≲35 K. For example, doubly shadowed terrain at 20 K would need to occupy 84% of the FOV (where the surrounding terrain is 40 K) (Fig. 7) to produce $\Re_{8/9} - \Re_{8/9\ model} = 0.2$ observed in Fig. 7.

For apparent temperatures ≲20 K the fewer number of observations of the PSR target results in poorer statistics, as evidenced by the widening of the standard deviation envelope (blue dashed line in Fig. 6). It is possible that the reduction in SNR with temperature for channel 8 makes values of $\Re_{8/9}$ more spurious for apparent temperatures ≲20 K. Nonetheless, even if we had confidence in values of $\Re_{8/9}$ at such temperatures, in the case of our model it is very unlikely that surface roughness could be the cause of $\Re_{8/9} - \Re_{8/9\ model} \gtrsim 0.5$.

5.2.1. Implications of micro-cold traps

While the existence of doubly-shadowed micro cold traps may come as no surprise given our understanding of lunar surface roughness (Bandfield et al., 2015), these results could indicate that observations of PSRs by Diviner contain thermal emission from ultra-cool surfaces that could be 10–15 K cooler than their surroundings.

For cold-trapped volatiles with an impact origin, selected compounds with low volatility temperatures from the distribution of those known to be present in comets (e.g. Cottin et al., 1999; Ehrenfreund and Charnley, 2000; Task Group on Organic Environments in the Solar System, 2007) and meteorites (Botta and Bada, 2002), such as simple organics and clathrates (Zhang and Paige, 2009), may be more relevant to the possible volatile inventory in these cooler micro cold traps.

As an example for one species, Hodges (1980) explored the processes by which exospheric argon could be cold-trapped in doubly-shadowed areas. Argon's cold-trapping temperature was found to be between ~40 and ~70 K depending on the substrate onto which it is adsorbed. Zhang and Paige (2009) found the temperature criterion for long-term stability of argon (<1 m of sublimation per billion years) to

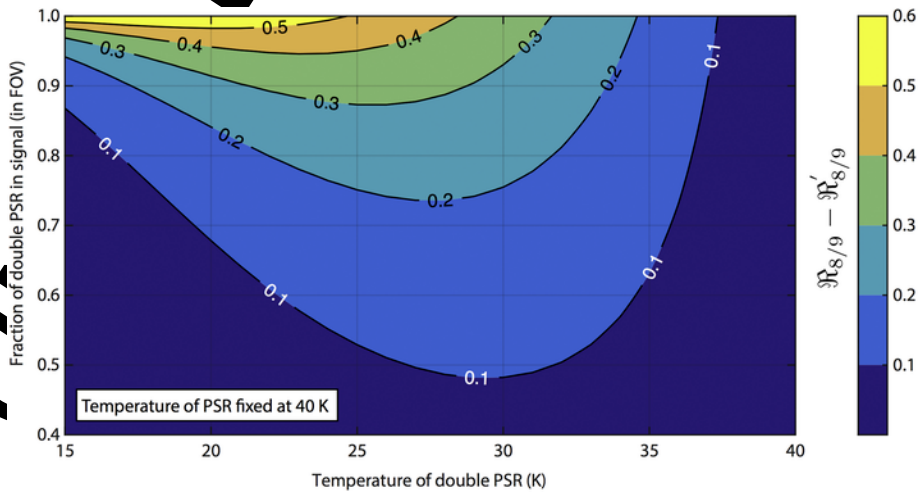

Fig. 7. Difference between $\Re_{8/9}$ modelled for a black body with uniform temperature at 40 K and that modelled for a surface with some fraction at a lower temperature, $\Re'_{8/9}$, plotted as a function of both the fraction of ultra-cold terrain in the field of view, and its temperature.

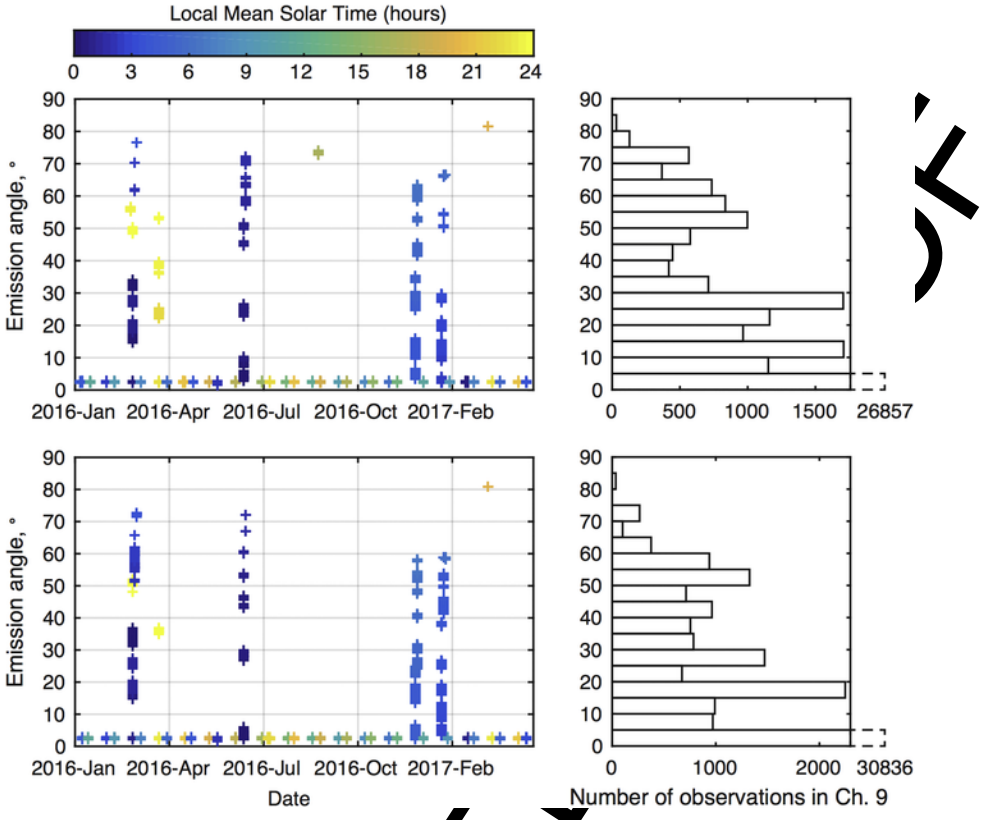

Fig. 8. Left – Date and emission angle of the boresight vectors for observations of the PSR (top) and non-PSR (bottom) targets in channel 9, colorized by local time. The inclusive time period is selected to highlight high emission angle observation campaigns. Channel 9 is selected as a representative example; the co-alignment of detectors ensures all channels have almost identical coverage. Note that high emission angle targeted observations were scheduled at night only. Right – Distribution of emission angle coverage for the two targets. Emission angle in this definition is not terrain-relative, but simply the angle between the boresight and lunar sphere. In our analysis we calculate the terrain relative emission angle, t_{emis}. (For interpretation of the references to color in this figure legend, the reader is referred to the web version of this article.)

be ~20 K. In the same study they asserted that, for organic compounds, volatility increases roughly linearly with molecular mass. It is clear that such complexities should be expected for all species and govern the emplacement and loss processes for volatiles in simple and complex-shadowed regions.

We assert that micro-cold traps may contribute to the observed differences between modelled and observed $\mathfrak{R}_{8/9}$, but they are not likely to be the sole cause. Thus we proceed to explore alternative potential sources of observation bias and effects that could cause changes in emission that may collectively combine to replicate the observed 'apparent' emissivity.

5.3. Emission angle

The vast majority of observations were acquired at low terrain-relative emission angles (t_{emis}) for both targets: ~80% of observations were acquired at $t_{emis} \leq 3^{\circ}$ and ~91% were acquired at $t_{emis} \leq 10^{\circ}$. However, some observations at higher emission angles were acquired as part of a specific campaign involved 'lock-on' targeting, where Diviner actuators were moved in intervals as the spacecraft passed over the targets to observe at a range of emission angles. These observations began as part of a campaign in March 2016 and are visible in Fig. 8 as observations closely spaced on the time axis.

To illustrate any trends over emission angle, we plot $\mathfrak{R}_{8/9} - \mathfrak{R}_{8/9\ model}$ as a function of t_{emis} (Fig. 9).

t_{emis} is specific to each triangular facet in the terrain model, and may differ between channels 8 and 9, even for observations in the same orbit. This is due to the spread of emission angles in EFOVs. To demonstrate; consider that some signal in an observation originates from a forward-looking part of a channel 8 EFOV, i.e. that is inclined from the boresight towards the spacecraft velocity vector. The same terrain (i.e. the same triangle in the DEM) may also radiate and contribute signal to the backward-looking part of a channel 9 EFOV. If only these portions of observations were binned, then the band ratio would not account for the difference in emission angle. It is important to reiterate however, that the fringes of EFOVs contribute far less signal to observations than the central portions. Consequently, while there is some scatter in the band ratio caused by the spread of emission angle within EFOVs, the origin of overall signal is heavily weighted towards the boresight, where emission angles in EFOVs from different channels are most similar.

Nonetheless, to quantify scatter in band ratio that may be caused by this effect, we calculate the 1σ on the distribution of emission angles in each bin (Fig. 9), and find in general that errors are comparable in size or smaller than bin width, equal to 2° in our analysis. Increased scatter at high emission angles, indicated by widening of the 1σ envelope in the distribution of $\mathfrak{R}_{8/9} - \mathfrak{R}_{8/9\ model}$ may be due to the combined effects of fewer observations at high emission angles, and the enlargement of the EFOV at high emission angles. With increasing emission angle, signal is contributed from wider areas, increasing the probability of mixing of thermal states within each observation and thus, spread in the calculated band ratios.

Theory suggests that for small values of the single scattering albedo, w, directional emissivity, ε_d, is 1 at all angles and the surface emits like a black body (Hapke, 2012). Therefore low-albedo materials can be assumed to have emissivity that is not dependent on emission angle. This is supported by measurements of sand and playa surfaces by Jankowsky and Jacobson (1990). Our observation of invariant emissiv-

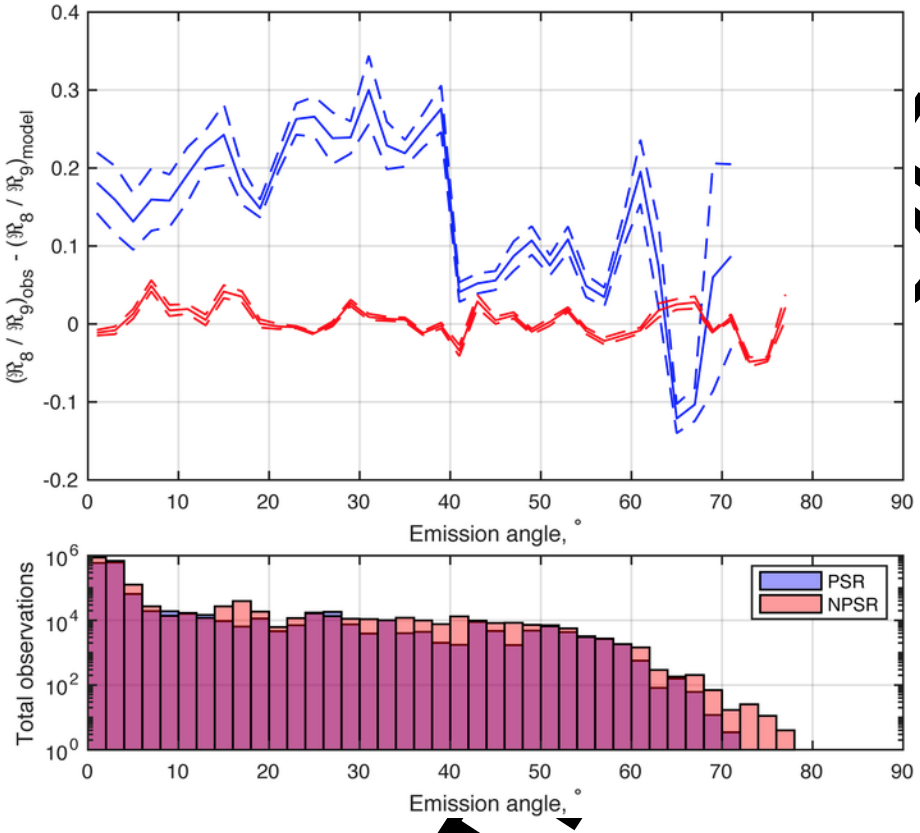

Fig. 9. Top – $\Re_{8/9} - \Re_{8/9\ model}$ as a function of terrain-relative emission angle (t_{emis}) for each target. Dashed lines indicate $\pm 1\sigma$. Bottom – Total number of observations (log-scale) in both channels 8 and 9, for each target, plotted as a function of t_{emis} in bins of 2°.

ity over emission angle of the NPSR target is generally consistent with it being made of a relatively low albedo material, but poor coverage at high emission angles (where a downturn in ε_d would be most prominent) precludes meaningful constraint of albedo.

While both targets suffer from greatly reduced coverage at high emission angles (≳55°), the PSR target exhibits a dramatic upturn in $\Re_{8/9} - \Re_{8/9\ model}$ for $t_{emis} \gtrsim 40°$. The region between 40–55° is not coincident with a reduction in observation coverage, but the relatively low overall number of lock-on observations in the off-nadir campaign makes this relationship sensitive to other relevant parameters that may influence $\Re_{8/9}$, and precludes meaningful comparison against a global nighttime emissivity trends (Bandfield et al., 2015), which result from averages of the global dataset and thus are less sensitive to bias that could be introduced by local time coverage of observations. Next, we investigate possible observation bias caused by local time.

5.4. Local time

The relationship between local time and $\Re_{8/9} - \Re_{8/9\ model}$ is intriguing (Fig. 10). Observation bias in local time is not expected to contribute to any trend, due to the generally even coverage of all nighttime hours for both targets.

$\Re_{8/9} - \Re_{8/9\ model}$ for the non-PSR target exhibits no apparent dependence on local time and shows only small deviations from 0 over the entire lunar night, consistent with invariance in the far-IR emissivity for this target; also apparent as a function of temperature and emission angle (Figs. 6 and 9).

Results for the PSR target are dramatically different, however. Short timescale noise on the difference between the modelled and observed band ratio appears to superimpose a broad trend throughout the polar night. At sunset, results for the PSR target are similar to the NPSR target, but increasing $\Re_{8/9} - \Re_{8/9\ model}$ reaches a maximum in mid-night, ~02:00 (Fig. 10), then declines towards sunrise. This implies that a relative reduction in apparent ch. 9 emissivity compared to ch. 8 (or increase in ch. 8 relative to ch. 9) occurs during the night for the PSR target only. Importantly, this time period is when the PSR target is at its coldest (Fig. 3), with mean temperatures dropping below ~40 K. This temperature regime is where we also observe a dramatic increase in $\Re_{8/9} - \Re_{8/9\ model}$ (Fig. 6). We surmise therefore that this diurnal feature could simply be a further manifestation of an effective temperature-dependence in apparent emissivity ratio that we observe.

5.5. Insights from thermal conductivity measurements

The thermal inertia of lunar regolith causes the amplitude of the diurnal thermal wave to taper rapidly with depth in the top ~10 cm (Hayne et al., 2017), but at the surface and at sub-mm scales, thermal equilibration would occur very quickly.

On average, channel 9 can sense signal from several hundred microns deeper in PSR regolith than channel 8, and any differences in temperature over that short distance could lead to detection of anisothermality in the vertical direction. However, we do not expect to find significant temperature gradients in lunar regolith between the sensing depths of channels 8 and 9. If such gradients were contributors to the signal we observe then (i) they would need to be significant over the difference in sensing depths between channels 8 and 9, a few hundred microns, and (ii) an explanation would then be required for the absence of any local time dependence of $\Re_{8/9} - \Re_{8/9\ model}$ for the NPSR target (Fig. 10), particularly at dawn and dusk, when temperatures can change by >100 K over relatively short timescales (Fig. 2) and should invoke steep thermal gradients. The absence of evidence for such a dependence suggests that vertical anisothermality is probably not the cause of the observed differences between PSR and NPSR far-IR band ratios.

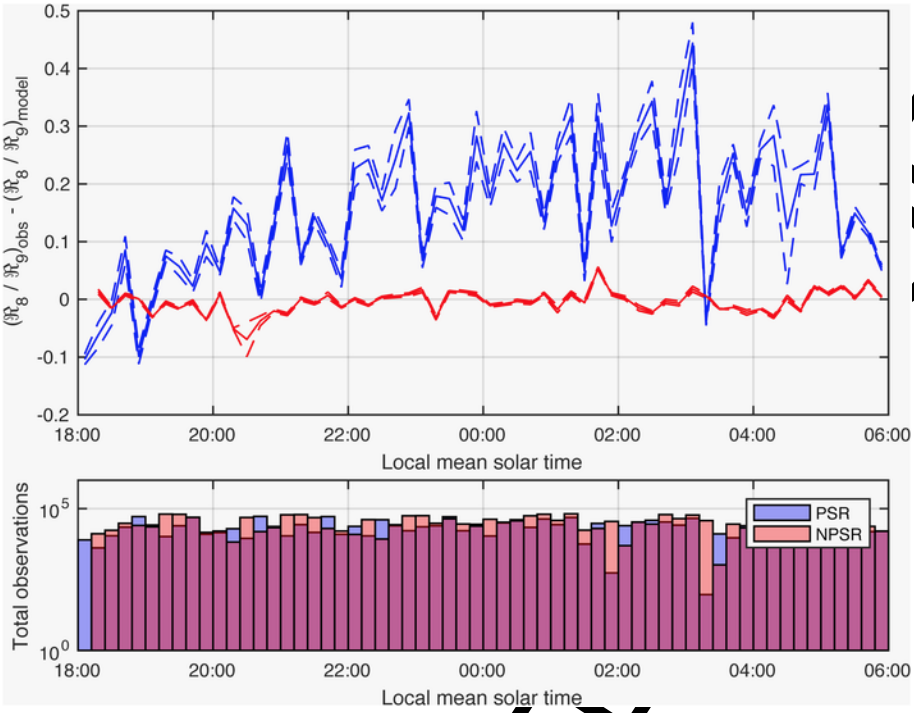

Fig. 10. Top – $\Re_{8/9}$ - $\Re_{8/9\ model}$ as a function of local mean solar time for each target. Dashed lines indicate $\pm 1\sigma$. Bottom – Total number of observations (log-scale) in both channels 8 and 9, for each target, plotted as a function of local time (in bins of 12 min).

Instead, differences in density between an uppermost and immediately underlying layer could produce differences in thermal conductivity, and therefore steeper gradients in thermophysical parameters in the near surface.

The reduction of thermal conductivity with decreasing density (e.g. Fountain and West, 1970) may be important here to explain the trend in the 40–59 K temperature interval where $\Re_{8/9} - \Re_{8/9\ model}$ is flat, but non-zero for the PSR target (Fig. 6): The presence of a thin veneer of water frost, or simply lower density of PSR regolith compared to non-PSR regolith, could be consistent with this.

However, this effect alone would not contribute to the apparent temperature dependence of $\Re_{8/9} - \Re_{8/9\ model}$ below 40 K (Fig. 6), which we find could be at least partially caused by sub-FOV doubly-shadowed terrain (Fig. 7). Siegler et al. (2016) assert that the variation of thermal conductivity as a function of temperature is inherently linked to the crystallinity of a given material, and published laboratory measurements that indicate that both Apollo 11 regolith and regolith simulant NU-LHT-2M, show thermal conductivity consistent with amorphous crystalline structure, as modelled by Woods-Robinson et al. (2019), rather than crystalline materials.

If a thin layer of surface material possesses thermophysical properties with different temperature-dependencies than the bulk material below, then steeper thermal gradients would exist near the surface and result in larger differences between ch. 8 and ch. 9 brightness temperatures due to their different sensing depths, and a larger deviation in $\Re_{8/9} - \Re_{8/9\ model}$, as we observe (Fig. 8).

A lack of data in the literature quantifying the effect of ice-regolith mixtures on far-IR emissivity precludes our ability to quantify the expected change on $\Re_{8/9}$ by surface ice compared to dry regolith. Nonetheless, a thin veneer of water frost, as indicated by previous studies for the PSR target (Hayne et al., 2015; Fisher et al., 2017) remains consistent with our observations, because differential rates of change in thermal conductivity would occur between an immediate subsurface regolith layer and uppermost volatile layer as a function of temperature.

6. Conclusions

The radiance ratio between Diviner channels 8 and 9, when corrected for known instrumental and geometric effects, shows apparent differences between normally illuminated and permanently shadowed targets in Amundsen crater. The use of only nighttime data in our analysis leads us to infer this is caused by the two surfaces having different emissivity curves in the far-IR.

The PSR target shows apparent emissivity ~100–400 μm (channel 9) lower than expected relative to that between 50 and 100 μm (channel 8). The magnitude of the differential increases with decreasing temperature below about 40 K. We do not suspect observation bias to be a factor between 30 and 40 K. For surfaces between 50–70 K, the non-PSR target shows emissivity that is predicted well by a simple Planck radiance model that incorporates the quantum efficiencies of both bandpasses, indicating no differential emissivity in the far-IR.

Via a simple thermal emission model, in which a bimodal temperature distribution is observed by a finite FOV, we demonstrate that it is possible to produce observable anisothermality in the PSR target's anomalous far-IR emissivity curve with the presence of sub-FOV scale cold traps. Such doubly-shadowed terrain could be produced by typical lunar surface roughness in PSRs not more than ~0.45 areal fraction. However, according to our 2-component thermal emission model, the magnitude of anisothermality that is likely, even for high surface roughnesses, is unable to explain our observations of the far-IR emission curve.

We find inconclusive evidence for emissivity dependence on terrain-relative emission angle, as is theorized for two-layer particulate surfaces, because data coverage is poorest at high emission angles, where the signal would be most obvious. In addition, an apparent broad trend in emissivity with local time for the PSR target may simply be a proxy for the temperature dependence.

Finally, we surmise that the ratio of Diviner far-IR channels 8 and 9, when corrected for all known geometric and instrumental effects,

may indicate the combined impact on apparent emissivity of two physical properties of PSR surfaces: 1. The abundance of sub-FOV doubly-shadowed terrain harbouring ultra-cool temperatures, and 2. The thermophysical gradient in the uppermost layers of PSR regolith that may be caused by a thin veneer of water ice.

Acknowledgements

Authors thank the NASA Lunar Reconnaissance Orbiter program and Diviner operations team at NASA Goddard Space Flight Center, NASA/Caltech Jet Propulsion Laboratory, and the University of California Los Angeles for providing data for this research. Special thanks to Marco Delbo for fruitful discussions regarding IR emissivity, and to two reviewers for helpful comments and suggestions that improved the paper. Elliot Sefton-Nash was supported by the European Space Agency. Finally, we remember and celebrate our colleague and friend, Joshua L. Bandfield, who passed during publication of this work. Josh's compassionate life, pursuit of truth, and profound contributions to planetary science remain inspirational.

Appendix A.

Following Williams et al. (2016), the EFOV is modelled as a Monte Carlo distribution of points in the focal plane. We here describe the change from the instrument/spacecraft-relative coordinate systems in which EFOV points are defined, to 'lunar body-fixed' coordinate system. This must be performed on each point to enable ray-tracing to determine intersection of EFOVs with the lunar digital elevation model (Teanby, 2009).

Each Monte Carlo point in the EFOV represents a fraction $1/n_{efov}$ of the total observation. For this study $n_{efov} = 1000$. Each point is defined as a unit ray with one end at the detector (the start of the boresight), but that is angularly offset from the boresight at the target end. Angular offsets of the ray from the boresight are in the cross and in-track directions, i.e. parallel and perpendicular, respectively, to the direction of each channels' linear detector array. These angular offsets are treated as spherical coordinates, which allows us to convert each unit look vector into Cartesian coordinates:

$$\boldsymbol{R}_D = x\hat{\boldsymbol{h}} + y\hat{\boldsymbol{k}} + z\hat{\boldsymbol{l}}$$

where the unit basis vectors of each component form the detector reference frame, $\boldsymbol{D}$:

$$\boldsymbol{D} = \left\{\hat{\boldsymbol{h}}, \hat{\boldsymbol{k}}, \hat{\boldsymbol{l}}\right\}$$

In this right-handed frame, $\hat{\boldsymbol{h}}$ is the boresight, $\hat{\boldsymbol{k}}$ is defined as perpendicular to the direction of the linear detector arrays, and $\hat{\boldsymbol{l}}$ is aligned with the linear detector arrays (see Paige et al., 2010b for details). During nominal nadir mapping mode $\hat{\boldsymbol{k}}$ is the direction of spacecraft travel, i.e. the in-track direction, while $\hat{\boldsymbol{l}}$ is the cross-track direction. We must compute the intersection of each EFOV point with the terrain model, which is stored in the body-fixed lunar reference frame, $\boldsymbol{B}$. Due to the fact that $\boldsymbol{B}$ is the reference frame of the digital elevation model (DEM) that we want to convert EFOV rays into, its component vectors $\{\hat{\boldsymbol{p}}, \hat{\boldsymbol{q}}, \hat{\boldsymbol{r}}\}$ form a 3 × 3 identity matrix:

$$\boldsymbol{B} = \{\hat{\boldsymbol{p}}, \hat{\boldsymbol{q}}, \hat{\boldsymbol{r}}\} = \begin{matrix} 1 & 0 & 0 \\ 0 & 1 & 0 \\ 0 & 0 & 1 \end{matrix}$$

We construct a change of basis matrix, $\boldsymbol{P}_{\boldsymbol{B}\leftarrow\boldsymbol{D}}$, to convert coordinates from $\boldsymbol{D}$ to $\boldsymbol{B}$, which reduces simply to the components of $\boldsymbol{D}$:

$$\boldsymbol{P}_{B\leftarrow D} = \begin{matrix} \hat{\boldsymbol{h}}.\hat{\boldsymbol{p}} & \hat{\boldsymbol{h}}.\hat{\boldsymbol{q}} & \hat{\boldsymbol{h}}.\hat{\boldsymbol{r}} \\ \hat{\boldsymbol{k}}.\hat{\boldsymbol{p}} & \hat{\boldsymbol{k}}.\hat{\boldsymbol{q}} & \hat{\boldsymbol{k}}.\hat{\boldsymbol{r}} \\ \hat{\boldsymbol{l}}.\hat{\boldsymbol{p}} & \hat{\boldsymbol{l}}.\hat{\boldsymbol{q}} & \hat{\boldsymbol{l}}.\hat{\boldsymbol{r}} \end{matrix} = \begin{matrix} h_1 & h_2 & h_3 \\ k_1 & k_2 & k_3 \\ l_1 & l_2 & l_3 \end{matrix}$$

Each EFOV ray is then converted from the detector frame to the lunar body-fixed frame via multiplication with the change of basis matrix:

$$\boldsymbol{R}_B = \boldsymbol{R}_D.\boldsymbol{P}_{B\leftarrow D} = \begin{matrix} xh_1 & yh_2 & zh \\ xk_1 & yk_2 & z \\ xl_1 & yl_2 & z \end{matrix}$$

Since we cannot know at this stage the precise distance required for intersection of the EFOV ray with the moon's surface, we extend $\boldsymbol{R}_B$ by multiplying it by a very large factor, s, such that $|s\boldsymbol{R}_B|$ is never too short to intersect with the DEM when an intersection would occur for a ray of infinite length.

References

Bandfield, J.L., Hayne, P.O., Williams, J.-P., Greenhagen, B.T., Paige, D.A., 2015. Lunar surface roughness derived from LRO Diviner Radiometer observations. Icarus 248, 357–372. https://doi.org/10.1016/j.icarus.2014.11.009.

Botta, O., Bada, J.L., 2002. Extraterrestrial organic compounds in meteorites. Surv. Geophys. 23, 411–467. https://doi.org/10.1023/A:1020139302770.

Clark, J.M., Migliorini, A., Barucci, A., Segura, M., 2006. Constraining the surface properties of Saturn's icy moons, using Cassini/CIRS emissivity spectra. Icarus 187, 574–3[illegible]. https://doi.org/10.1016/j.icarus.2006.09.008.

Colaprete, A., Schultz, P., Heldmann, J., Wooden, D., Shirley, M., Ennico, K., Hermalyn, B., Marshall, W., Ricco, A., Elphic, R.C., Goldstein, D., Summy, D., Bart, G.D., Asphaug, E., Korycansky, D., Landis, D., Sollitt, L., 2010. Detection of water in the LCROSS ejecta plume. Science 330, 463–468. https://doi.org/10.1126/science.1186986.

Cottin, H., Gazeau, M.C., Raulin, F., 1999. Cometary organic chemistry: a review from observations, numerical and experimental simulations. Planet. Space Sci. 47, 1141–1162. https://doi.org/10.1016/S0032-0633(99)00024-0.

Delaunay, B., 1934. Sur la sphère vide. vol. 7, Otdelenie Matematicheskikh i. Estestvennykh Nauk, 793–800.

Ehrenfreund, P., Charnley, S.B., 2000. Organic molecules in the interstellar medium, comets, and meteorites: a voyage from dark clouds to the early Earth. Annu. Rev. Astron. Astrophys. 38, 427–483. https://doi.org/10.1146/annurev.astro.38.1.427.

Fisher, E.A., Lucey, P.G., Lemelin, M., Greenhagen, B.T., Siegler, M.A., Mazarico, E., Aharonson, O., Williams, J.-P., Hayne, P.O., Neumann, G.A., Paige, D.A., Smith, D.E., Zuber, M.T., 2017. Evidence for surface water ice in the lunar polar regions using reflectance measurements from the Lunar Orbiter Laser Altimeter and temperature measurements from the Diviner Lunar Radiometer Experiment. Icarus 292, 74–85. https://doi.org/10.1016/j.icarus.2017.03.023.

Fountain, J.A., West, E.A., 1970. Thermal conductivity of particulate basalt as a function of density in simulated lunar and Martian environments. J. Geophys. Res. 75 (20), 4063–4069.

Gladstone, G.R., Stern, S.A., Retherford, K.D., Black, R.K., Slater, D.C., Davis, M.W., Versteeg, M.H., Persson, K.B., Parker, J.W., Kaufmann, D.E., Egan, A.F., Greathouse, T.K., Feldmann, P.D., Hurley, D., Pryor, W.R., Hendrix, A.R., 2010. LAMP: the lyman alpha mapping project on NASA's lunar reconnaissance orbiter mission. Space Sci. Rev. 150 (1–4), 161–181. https://doi.org/10.1007/s11214-009-9578-6.

Hapke, B., 2012. Theory of Reflectance and Emittance Spectroscopy. Cambridge University Press. ISBN: 978-0-521-88349-8.

Hayne, P.O., Hendrix, A., Sefton-Nash, E., Siegler, M.A., Lucey, P.G., Retherford, K.D., Williams, J.-P., Greenhagen, B.T., Paige, D.A., 2015. Evidence for exposed water ice in the moon's south polar regions from lunar reconnaissance orbiter ultra-violet albedo and temperature measurements. Icarus 255, 58–69. https://doi.org/10.1016/j.icarus.2015.03.032.

Hayne, P.O., Ingersoll, A.P., Paige, D.A., Aharonson, O., Alkalai, L., Byrne, S., Chen, Y., Cohen, B., Colaprete, A., Combe, J.-P., Edwards, C., Ehlmann, B., Feldman, W., Foote, E., Greenhagen, B.T., Hendrix, A., Hermalyn, B., Liu, Y., Lucey, P.G., Malphrus, B., McClanahan, T.P., McCleese, D.J., McCord, T.B., Neish, C., Neumann, G., Nuno, R., Pilorget, C., Poston, M., Sanders, G., Schorghofer, N., Sellar, R.G., Siegler, M., Staehle, R., 2014. New Approaches to Lunar Ice Detection and Mapping. Keck Institute for Space Studies.

Hayne, P.O., Bandfield, J.L., Siegler, M.A., Vasavada, A.R., Ghent, R.R., Williams, J.-P., Greenhagen, B.T., Aharonson, O., Elder, C.M., Lucey, P.G., Paige, D.A., 2017. Global regolith thermophysical properties of the Moon from the Diviner Lunar Radiometer Experiment. Journal of Geophysical Research: Planets 122, 2371–2400. https://doi.org/10.1002/2017JE005387.

Li, S., Lucey, P.G., Milliken, R.E., Hayne, P.O., Fisher, E., Williams, J.-P., Hurley, D.M., Elphic, R.C., 2018. Direct evidence of surface exposed water ice in the lunar polar regions. Proc. Natl. Acad. Sci. U. S. A. 115 (36), 8907–8912. https://doi.org/10.1073/pnas.1802345115.

Mazarico, E., Neumann, G.A., Smith, D.E., Zuber, M.T., Torrence, M.H., 2011. Illumination conditions of the lunar polar regions using LOLA topography. Icarus 211, 1066–1081. https://doi.org/10.1016/j.icarus.2010.10.030.

, . .

Moore, M.H., Hudson, R.L., 1992. Far-infrared spectral studies of phase changes in water ice induced by proton irradiation. Astrophys. J. 401, 353–360.

Paige, D.A., Foote, M.C., Greenhagen, B.T., Schofield, J.T., Calcutt, S.B., Vasavada, A.R., Preston, D.J., Taylor, F.W., Allen, C.C., Snook, K.J., Jakosky, B.M., Murray, B.C., Soderblom, L.A., Jau, B., Loring, S., Bulharowski, J., Bowles, N.E., Thomas, I.R., Sullivan, M.T., Avis, C., De Jong, E.M., Hartford, W., McCleese, D.J., 2010. The lunar reconnaissance orbiter diviner lunar radiometer experiment. Space Sci. Rev.https://doi.org/10.1007/s11214-0 09-9529-2.

Paige, D.A., Siegler, M.A., Zhang, J.A., Hayne, P.O., Foote, E.J., Bennett, K.A., Vasavada, A.R., Greenhagen, B.T., Schofield, J.T., McCleese, D.J., Foote, M.C., DeJong, E., Bills, B.G., Hartford, W., Murray, B.C., Allen, C.C., Snook, K., Soderblom, L.A., Calcutt, S., Taylor, F.W., Bowles, N.E., Bandfield, J.L., Elphic, R., Ghent, R., Glotch, T.D., Wyatt, M.B., Lucey, P.G., 2010. Diviner Lunar Radiometer observations of cold traps in the Moon's south polar region. Science 330 (6003), 479–482. https://doi.org/10.1126/science.1187726.

Rubanenko, L., Aharonson, O., 2017. Stability of ice on the Moon with rough topography. Icarus 296, 99–109. https://doi.org/10.1016/j.icarus.2017.05.028.

Schultz, P.H., Hermalyn, B., Colaprete, A., Ennico, K., Shirley, M., Marshall, W.S., 2010. The LCROSS cratering experiment. Science 330 (6003), 468–472. https://doi.org/10.1126/science.1187454.

Sefton-Nash, E., Williams, J.-P., Greenhagen, B.T., Aye, K.-M., Paige, D.A., 2017. Diviner lunar radiometer gridded brightness temperatures from geodesic binning of modeled fields of view. Icarus 298, 98–110. https://doi.org/10.1016/j.icarus.2017.04.007.

Seidelmann, P.K., Abalakin, V.K., Bursa, M., Davies, M.E., de Bergh, C., Lieske, J.H., Oberst, J., Simon, J.L., Standish, E.M., Stooke, P., Thomas, P.C., 2002. Report of the IAU/IAG working group on cartographic coordinates and rotational elements of the planets and satellites: 2000. Celest. Mech. Dyn. Astron. 82 (1), 83–111.

Siegler, M., Zhong, F., Woods-Robinson, R., Paige, D.A., 2016. Low temperature (<100K) regolith thermal conductivity - preliminary laboratory data. In: American Geophysical Union, Fall General Assembly 2016, Abstract P24A-05.

Smith, D., 2017. Lunar Orbiter Laser Altimeter Dataset: LRO-L-LOLA-4-GDR-V1.0. Planetary Data System.

Task Group on Organic Environments in the Solar System, 2007. Exploring Organic Environments in the Solar System. National Academies Press, Washington, D. C.

Teanby, N.A., 2006. Intersection between spacecraft viewing vectors and digital elevation models. Comput. Geosci. 33, 1166–57. https://doi.org/10.1016/j.cageo.2007.11.007.

Woods-Robinson, R., Siegler, M.A., Paige, D.A., . A Model for the Thermophysical Properties of Lunar Regolith at Low Temperatures, *Journal of Geophysical Research: Planets*, 2019, Accepted manuscript. https://doi.org/10.1029/2019JE005955.().